JACS
JOURNAL OF THE AMERICAN CHEMICAL SOCIETY

ARTICLE

pubs.acs.org/JACS

Using Atomic Layer Deposition to Hinder Solvent Decomposition in Lithium Ion Batteries: First-Principles Modeling and Experimental Studies

Kevin Leung,*[,†] Yue Qi,[‡] Kevin R. Zavadil,[†] Yoon Seok Jung,[§,¶] Anne C. Dillon,[§] Andrew S. Cavanagh,[∥] Se-Hee Lee,[⊥] and Steven M. George[#]

[†]Sandia National Laboratories, MS 1415 and 0888, Albuquerque, New Mexico 87185, United States

[‡]General Motors R&D Center, Warren, Michigan 48090, United States

[§]National Renewable Energy Laboratory, Golden, Colorado 80401, United States

[∥]Department of Physics, [⊥]Department of Mechanical Engineering, and [#]Department of Chemistry and Biochemistry, University of Colarado, Boulder, Colorado 80309, United States

[¶]Interdisciplinary School of Green Energy, Ulsan National Institute of Science and Technology (UNIST), Ulsan 689-798 South Korea

Supporting Information

ABSTRACT: Passivating lithium ion (Li) battery electrode surfaces to prevent electrolyte decomposition is critical for battery operations. Recent work on conformal atomic layer deposition (ALD) coating of anodes and cathodes has shown significant technological promise. ALD further provides well-characterized model platforms for understanding electrolyte decomposition initiated by electron tunneling through a passivating layer. First-principles calculations reveal two regimes of electron transfer to adsorbed ethylene carbonate molecules (EC, a main component of commercial electrolyte), depending on whether the electrode is alumina coated. On bare Li metal electrode surfaces, EC accepts electrons and decomposes within picoseconds. In contrast, constrained density functional theory calculations in an ultrahigh vacuum setting show that, with the oxide coating, e^- tunneling to the adsorbed EC falls within the nonadiabatic regime. Here the molecular reorganization energy, computed in the harmonic approximation, plays a key role in slowing down electron transfer. Ab initio molecular dynamics simulations conducted at liquid EC electrode interfaces are consistent with the view that reactions and electron transfer occur right at the interface. Microgravimetric measurements demonstrate that the ALD coating decreases electrolyte decomposition and corroborates the theoretical predictions.

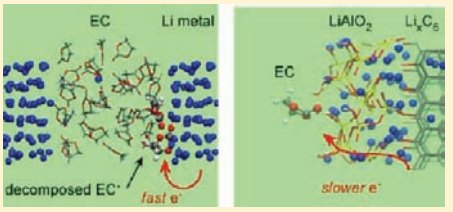

I. INTRODUCTION

Improving the fundamental scientific understanding of lithium ion batteries[1−3] is critical for electric vehicles and other energy storage technologies. A key feature that enables the use of negative electrodes (graphite, Li metal, Si, Sn) operating below the reduction voltage of current commercial electrolytes is the formation of an electronically passivating but Li^+-conducting solid electrolyte interphase (SEI) film on electrode surfaces.[1−5] Battery performance, irreversible capacity "loss," power fade, durability, exfoliation of graphite, and safety are highly dependent on the quality of the SEI. Therefore understanding the nature, formation composition, structure, and property of SEI is of great interest for Li ion batteries. In this work, we apply computational and experimental techniques to analyze the success of the conformal atomic layer deposition (ALD) strategy for creating a passivating layer ("artificial SEI") on electrodes,[6−10] focusing on graphitic carbon anodes.[11]

It is generally accepted that, upon the first charge of uncoated graphitic anodes, the negative potential applied to induce Li^+ intercalation into graphite decomposes ethylene carbonate (EC) molecules in the solvent, yielding a self-limiting, 3−10 nm thick, passivating SEI layer containing Li_2CO_3, lithium ethylene dicarbonate ($(CH_2CO_3Li)_2$),[2,4,5] and salt decomposition products. Early modeling work on organic solvent breakdown has focused on reactions inside bulk liquid regions, with an excess electron already injected.[12−15] While providing extremely useful predictions pertinent to that regime, such models necessarily ignore the possibility of surface-assisted reactions and the effects arising from electron transfer from electrodes. A more rigorous if costly technique, ab initio molecular dynamics (AIMD), has recently been applied to simulate chemical reactions at several explicit solid−liquid interfaces.[16−20] One of the authors' previous AIMD works follows chemical reactions in real time at the pristine graphitic anodes/liquid EC interface.[21,22] It is found that, at the initial stage of SEI formation, fast e^- transfer and kinetically controlled EC electrochemical reactions occur to form either CO or C_2H_4 gas,[23−26] mostly right at the oxidized edges of graphite sheets.[27,28]

Received: June 2, 2011
Published: July 28, 2011

As electrolyte decomposition proceeds, e^- transfer becomes impeded by the intervening and partially formed SEI layer between the solvent and the electrode, and the decomposed solvent fragments can no longer anchor directly to the pristine electrode surface. This important next stage should figure equally prominently in the overall solvent breakdown mechanism and the structure of naturally formed SEI. The electron tunneling blockage by SEI layers is a kinetic (not thermodynamic) phenomenon, akin to stoppage of electron leakage through gate-oxide dielectric in semiconductor devices.[29] Theoretical study there is hindered by the substantial thickness, possibly porous/gel-like nature, and the heterogeneous composition of natural SEI.[1−3,30]

Recently, it has been demonstrated that a subnanometer thick alumina layer created by the conformal ALD technique on graphite drastically diminishes solvent decomposition but permits lithium ion transport.[11] This promising ALD strategy even enables the cycling of low melting point propylene carbonate (PC), which otherwise exfoliates and destroys uncoated graphitic anodes. The mechanism of ALD electrode passivation has not been completely understood. While expected to block or slow down electron transfer from the electrode to the solvent, it also appears to enhance the mechanical properties of the electrodes[6] and likely hinders solvent intercalation between graphite sheets, thus preventing exfoliation. Apart from the technological implications, the unprecedented control over coating thickness and chemistry means that the ALD strategy also provides robust platforms for basic science studies of interfacial solvent decomposition reaction mechanisms and for electron tunneling through the insulating layer, which is a prerequisite for electrolyte breakdown.

In particular, the extreme thinness of ALD coatings lends itself to the present, predominantly first-principles computational study of electrode/solvent interfaces comprising up to 850 atoms. Using crystalline, hydroxylated $LiAlO_2$ layers as models of ALD coatings, we apply DFT and related theoretical techniques to show that ALD oxide films yield varying energetic, kinetic, and electron-tunneling impedance toward EC breakdown, depending on the surface Li content and oxide thickness. We also provide evidence that e^- transfer occurs to EC molecules immediately next to electrode surfaces. Because these molecules are deep within the electric double layer (EDL), screening of electric fields by the EDL is less effective. In this sense, EC decomposition at battery anodes can differ fundamentally from classic electrochemical redox paradigms, where well-solvated transition-metal complexes are separated by several angstroms from the electrodes and "outer-shell" e^- tunneling dominates.[31] The solvent decomposition processes on ALD coatings provide insights that may be extrapolated to other passivation strategies, including natural SEI formed from electrolyte breakdown.

Two limiting regimes of electron transfer, and two corresponding computational methods, are emphasized. Rigorously, DFT deals with the electronic ground state, with nuclear trajectories "adiabatic" to electronic configurations (i.e., ionic motions are slow compared with electron transfer). EC breakdown on Li (100) metal surface is in this adiabatic regime. DFT should be adequate for such processes, provided that the desired electronic configuration is the ground state and the self-interaction error of the approximate functional used is not critical to the properties being investigated.[32−36]

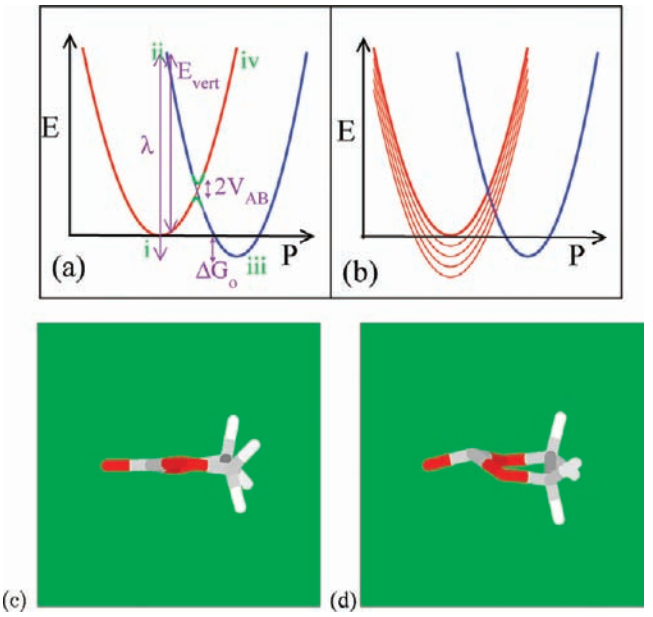

Figure 1. (a) Schematic of electron transfer between isolated orbitals. The red and blue represent the diabatic potential energy surfaces of e^- donor and acceptor as a function of the generalized polarization (P) degree of freedom. The green segments represent adiabatic processes with the noncrossing surfaces split by $2V_{AB}$. ΔG_o is the reaction free energy, and λ is the reorganization energy. The green roman numbers denote: (i) flat EC; (ii) flat EC^-; (iii) bent EC^-; and (iv) bent EC. (b) Nonadiabatic e^- transfer from a metallic electrode. The thick upper red line represents the Fermi level and is the primary donor orbital within cDFT calculations. Depicted as thin red lines, e^- can also transfer from the continuum of electrode donor states below the Fermi level, to the acceptor orbital, with however increased nonadiabatic barriers (crossing points between blue and red curves). (c and d) Flat and bent EC molecules, respectively. Red, gray, and white refer to O, C, and H atoms, respectively.

In the opposite, nonadiabatic regime,[37−41] e^- transfer or tunneling is slow on the time scale of nuclear motion, and one must keep track of two electronic surfaces.[31] The oxide-coated model electrodes considered in this work pertain to this latter limit, where the electron-transfer rate between two discrete orbitals is given by[42]

$$k_{et} = \frac{\sqrt{\pi}|V_{AB}|^2}{\hbar\sqrt{\lambda k_B T}} \exp\left[-\frac{(\Delta G_o + \lambda)^2}{4\lambda k_B T}\right] \quad (1)$$

where λ is the reorganization (free) energy, V_{AB} is the coupling matrix element connecting the two electronic surfaces, and ΔG_o is the reaction free energy. λ indicates the energy cost associated with molecular deformation needed to take on an extra electron ($EC \rightarrow EC^-$). V_{AB} is the familiar prefactor that depends on the overlap between two many-body wave functions associated with the two electronic surfaces (Figure 1a). Small V_{AB} correlates with nonadiabatic e^- tunneling.

Neither V_{AB} nor λ can be directly obtained using standard DFT methods. In this work, λ is estimated using the constrained DFT (cDFT) approach[38,43] and the Marcus theory harmonic construction (Figure 1a) under both ultrahigh vacuum (UHV) and liquid state[44,45] configurations. cDFT is also applied to estimate V_{AB}.[39] While cDFT and related methods have been applied to molecules on metal surfaces,[46−48] calculating V_{AB}

Table 1. Details of Systems Used in AIMD and Geometry Optimization plus NEB Barrier Calculations[a]

system/coating	method	Figure	stochiometry	cell size	N_{EC}
thin $LiAlO_2$	NEB	4c and d, 6	$Al_{48}Li_{96}O_{148}C_{92}H_{24}$	40.00 × 12.47 × 15.06	1
thick $LiAlO_2$	NEB	NA	$Al_{72}Li_{118}O_{208}C_{92}H_{24}$	46.0 × 12.47 × 15.06	1
thick $LiAlO_2$	AIMD	2d	$Al_{72}Li_{118}O_{208}C_{92}H_{24}$	48.5 × 12.47 × 15.06	36
thin $LiAlO_2$	AIMD	2e	$Al_{48}Li_{96}O_{148}C_{92}H_{24}$	43.00 × 12.47 × 15.06	36
only $LiAlO_2$	NEB	NA	$Al_{36}Li_{36}O_{84}H_{24}$	24.00 × 12.47 × 15.06	1
Al_2O_3	AIMD	2f	$Al_{72}O_{204}C_{120}H_{72}Li_{51}$	33.34 × 14.97 × 18.82	36
Li (100)	AIMD	2b	Li_{96}	30.35 × 14.63 × 14.63	32
Li (100)	NEB	2c	Li_{96}	30.35 × 14.63 × 14.63	1
Li (100)	NEB	3b−d	Li_{48}	24.00 × 9.75 × 9.75	1

[a] The spatial dimensions are in Å. Stochiometry omits EC atoms in the liquid region.

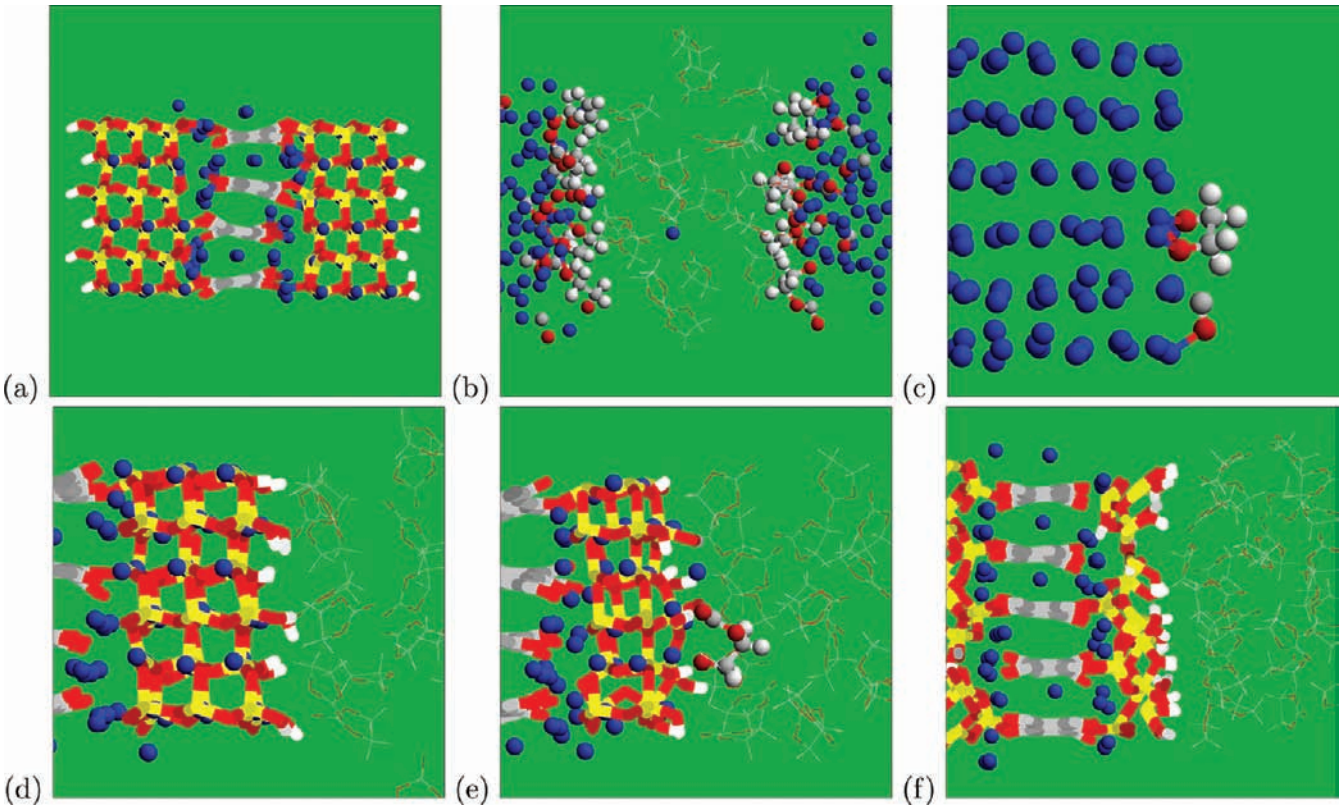

Figure 2. (a) Model electrode system with a narrow LiC_6 strip decorated with C═O edges and coated with a 10 Å thick $LiAlO_2$ layers terminated by hydroxyl groups. (b) A snapshot 15 ps into an AIMD trajectory of 32 EC molecules confined between Li metal (100) slabs conducted at T = 350 K. Li and decomposed EC are depicted as ball-and-stick models, intact EC as wireframes. (c) An isolated, decomposed EC on Li surface at T = 350 K, after a 7 ps AIMD simulation. (d) No decomposition on 10 Å thick $LiAlO_2$ coating after 7 ps. (e) One EC decomposed on 7 Å thick $LiAlO_2$-coated surface, T = 450 K, after 7 ps. (f) No decomposition on 5 Å thick, hydroxylated Al_2O_3 coating after 7 ps. Yellow, gray, red, blue, and white depict Al, C, O, Li, and H atoms, respectively.

between a metallic electrode and an e^--accepting molecule, or for that matter the total e^- tunneling rate, has relied on simplified models.[49−55] When augmented using a Fermi Golden-rule expression (Figure 1b), we argue that our V_{AB} value yields a well-defined kinetic prefactor for electron transfer from a metallic electrode. Our prefactor prediction is a preliminary estimate, and fundamental studies to extend cDFT to e^- transfer from metallic electrodes are needed. However, this is sufficient for our goal of order-of-magnitude estimates of e^- transfer rates. When the insulating layer (ALD oxide or natural SEI, or their combination) grows thicker, V_{AB} starts to decay with oxide thickness, and its magnitude is examined via extrapolation in a way analogous to the one-dimensional Wentzel−Kramers−Brillouin (WKB) formula. An alternative to this cDFT formulation may be Greens function/time-dependent DFT (TDDFT).[56−58] To our knowledge, TDDFT methods have not been successfully applied to predict orbital-to-orbital V_{AB} values that involve metallic electrodes.

dx.doi.org/10.1021/ja205119g |J. Am. Chem. Soc. 2011, 133, 14741–14754

With these computational techniques, we show that the subnanometer oxide coating,[7,11] generally not considered sufficiently thick for complete electron blockage in, say, gate oxide dielectric applications,[29] causes λ (much neglected in previous battery studies) to play a significant role in ALD-assisted passivation. Electron tunneling to EC, not bond breaking within the adsorbed molecule, is generally found to be the rate-determining step for breakdown of EC adsorbed on the ALD-coated electrode.

In terms of experiments, microgravimetric measurements that confirm the presence of solvent decomposition products on the surface are presented to corroborate aspects of our predictions.

This paper is organized as follows. Section II describes the methods used. Adiabatic electron-transfer induced EC reactions with Li metal surfaces is discussed in Section III. The long-range electron-transfer formalism is shown to be inapplicable here. Section IV describes the nonadiabatic electron tunneling from oxide-coated electrodes to EC molecules adsorbed on their surfaces and addresses the subsequent EC bond-breaking events. Adiabatic DFT/PBE calculations are shown to underestimate the electron tunneling barrier in this regime. Section V reports the experimental results, and Section VI briefly summarizes this work.

II. METHODS

A. Model Systems. The casual reader is encouraged to skip forward to Section III for the results.

The key model systems are ~7.0 ("thin") and ~10 Å ("thick") layers of $LiAlO_2$ in β-$NaAlO_2$ structure with (100) surface terminations, coated on narrow strips of Li_xC_6 electrodes (Table 1 and Figure 2; more details of this oxide phase are provided in the Supporting Information). Undercoordinated Al atoms on outer surfaces are terminated with OH groups, ensuring that surface states are removed. The oxide thickness is measured from Al to Al and excludes the surface hydroxyl groups or the C═O edge atoms originally residing on Li_xC_6. Crystalline $LiAlO_2$ is a solid-state electrolyte candidate material.[59] $LiAlO_2$ is used instead of Al_2O_3 to cover the possibility that the native Al_2O_3 layers deposited during ALD may have incorporated Li ions during the first charging half cycle. For example, some AlOH groups may be deprotonated at low voltages, causing Li^+ to coordinate to the AlO^- and become part of the surface. The $LiAlO_2$ mixed oxide thus allows us to examine surface composition effects on EC breakdown. The stochiometry of the coating is such that their formal charges sum to zero. Another research group has found $LiAlO_2$ signature on the surface of 5 nm thick ALD oxide films on Si anodes after power cycling using X-ray photo-electron spectroscopy.[60] Further computational evidence for Li incorporation into Al_2O_3 films is presented in the Supporting Information. If such Li^+ incorporation indeed occurs, then the ALD layer will expand beyond its original Al_2O_3 thickness.

The simulation cell, which provides a modest system size for AIMD simulations, is chosen so that the oxide is fairly well-matched to the Li_xC_6 surface cell, with oxide compressive strains of 1.8 and 5.7% in the two lateral dimensions. The crystalline models are idealized; as in gate-oxide dielectric materials, insulating oxides should be amorphous to minimize cracks. The amount of Li present in the graphite region is determined by tuning the Li chemical potential to 2.1 eV. Upon geometry optimization, Li ions initially residing at the C═O edges become strongly coordinated to the bottom surface of the oxide coating. Another model, with a single 10 Å thick layer of $LiAlO_2$ hydroxylated on both sides, but no Li_xC_6 component, is used to examine post e^- transfer EC^- bond breaking.

To emphasize the influence of surface groups, we also include a model with a ~5.0 Å thick layer of α-Al_2O_3 coated on both sides of the Li_xC_6 strip. The oxide layers have (0001) terminations with AlOH surface groups (Table 1). It has been predicted that γ-Al_2O_3 is more stable than the α phase for film thickness below 36 Å.[63] However, this estimate was made without accounting for surface hydroxylation. Since our thin Al_2O_3 film contains only two Al−O layers (not counting the C═O edge groups), the oxygen positions are arguably consistent with both α-Al_2O_3 with close-packed oxygen in ABAB stacking and cubic γ-Al_2O_3 with ABCABC stacking. In α-Al_2O_3, all Al are in octahedral sites, while Al occupies both octohedral and tetrahedral sites in γ-Al_2O_3. Upon applying geometry optimization to the initial "α-Al_2O_3" film, some Al ions are found to migrate to tetrahedral sites, especially those coordinated to graphite-edge C═O groups. Thus our "α-Al_2O_3" film arguably exhibits both α and γ character, consistent with experimental ALD coatings which are considered amorphous without long-range order.

Finally, a thin slab of lithium metal truncated along (100) surfaces is considered. Even though Li metal itself cannot currently be used as rechargeable anodes, EC breakdown products on Li are qualitatively similar to those on LiC_6 surfaces.[1,64] Under open circuit conditions, Li metal should be at a well-defined ~− 3 V versus the standard hydrogen potential.[65] Furthermore, EC decomposition on Li surface is free of the ambiguity associated with solvent cointercalation into graphite.[66] Thus Li metal provides an useful baseline with which to interpret predictions for the oxide-coated surfaces.

B. Adiabatic Regime: DFT, AIMD Simulations. All calculations are performed using the Vienna Atomic Simulation Package (VASP), version 4.6[67,68] and the Perdew−Burke−Ernzerhof (PBE) functional.[69] AIMD simulations apply Γ-point Brillouin zone sampling, a 400 eV planewave energy cutoff, and a 10^{-5} or 10^{-6} eV convergence criterion at each Born−Oppenheimer time step. The trajectories are kept at an average temperature of T = 450 K using Nose thermostats, except for the EC/Li metal simulation where T = 350 K is enforced. Tritium masses are substituted for protons to enable a time step of 1 fs. Under these conditions, the trajectories exhibit drifts of less than 1 K/ps. Due to the approximate nature of DFT functionals and the simulation protocol (tritium masses and thermostat used), the predicted reaction time scales should be treated as relative, not absolute. AIMD simulations reported do not account for spin polarization. Our previous work has revealed no qualitative difference between restricted singlet and spin-triplet DFT/AIMD simulations.[21] Molecular configurations are pre-equilibrated using Monte Carlo simulations and simple molecular force fields, as described in an earlier work.[21] Representative AIMD snapshots are depicted in Figure 2.

The AIMD liquid/solid interfacial simulations are akin to dipping electrodes fully preintercalated with Li into the organic solvent. In principle, it may be possible to intercalate Li^+ in the electrolyte, remove the anodes from solution, clean off possible decomposition products in inert environments, and reinsert in solution to measure the open circuit voltage. Such experiments have not been performed but can be attempted in the future. In Section IVD, we further discuss the electrochemical potential of these electrode models.

T = 0 K geometry optimizations and climbing image NEB[70] barrier calculations (e.g., Figure 3) are performed with spin polarization, a 10^{-4} eV convergence criterion, and a linear potential correction applied in the direction perpendicular to the surface to

remove dipole-image interactions.[71] Γ-point sampling is generally applied, except for calculations involving Li metal slabs where 1 × 2 × 2 Brillouin zone sampling is used. Even there, Γ-point NEB calculations yield a C−O bond-breaking barrier only 0.1 eV higher than the more dense Brillouin grid result. It is also found that the geometry and the net charge of an adsorbed, intact EC^- on $LiAlO_2$ coated graphite surface are unchanged whether Γ-point or 1 × 2 × 2 grids are used. Comparing restricted singlet and spin-polarization results, no difference is discernible in the EC on Li metal calculations, where the bond-breaking barrier is small (<0.1 eV, Section III) and the adiabatic electron transfer from the electrode and the bond-breaking event occur simultaneously. These are the conditions under which spontaneously EC decompositions are observed in picosecond AIMD simulations, justifying the use of nonspin-polarized DFT there. Higher bond-breaking barriers, like those on the 10 Å thick $LiAlO_2$ surface (see the Supporting Information), are reduced when spin polarization is allowed. A spot check shows that spin-unrestricted DFT calculations reduce the C_C−O cleavage barrier by 0.15 eV on this surface. Even with this reduction, the barrier is high enough to prevent observation of EC breakdown in picosecond time scale, and therefore using nonspin-polarized DFT in AIMD simulations does not affect the conclusion that no reactions occur within the 7 ps trajectories in high barrier cases. Further details on NEB calculations are discussed in the Supporting Information.

C. Nonadiabatic Regime: Constrained DFT. A version of the cDFT method[38,39] is implemented into VASP. The constraining potential is chosen to be

$$W(\mathbf{r}) = V_o[1 - \Pi_i f_i(\mathbf{r})] \quad (2)$$

$$f_i(\mathbf{r}) = [1 + \tanh(\kappa(|\mathbf{r} - \mathbf{r}_i| - w_i)]/2 \quad (3)$$

Here V_o is a constant to be self-consistently determined, κ is 6/Å, i labels the atoms in the selected EC participating in electron transfer, $\mathbf{r}_i$ is the atom position on that EC, and w_i is an element-specific radius and amounts to 1.65 Å for C and O and 1.25 Å for H. These values are similar to Lennard-Jones radii in simple atomic force fields. A more stringent wave function convergence criterion of 10^{-6} eV or smaller is enforced in self-consistent cDFT calculations. The $W(\mathbf{r})$ functional form does not double-count electron density on adjacent atoms and appears pertinent when bond breaking can occur. Normalized, atomic orbital-based charge projection operators used in the literature[38,45,72] may be less applicable for electron transfer coupled to bond breaking, but they can be tested for the present application in the future.

The total electronic charge on the selected EC is determined by projecting $W(\mathbf{r})/V_o$ on to the DFT electron density. With the w_i values mentioned above, unconstrained DFT predicts that a charge-neutral EC molecule adsorbed on the thin $LiAlO_2$ surface (Figure 4c) exhibits a slight +0.20 $|e|$ net charge, while −0.60 ± 0.1 $|e|$ resides on the EC^- (Figure 4d). The adsorbed EC^- exhibits a similar −0.67 $|e|$ charge on the $LiAlO_2$ oxide slab without any conductive Li_xC_6 component (Table 1). The non-integer values arise because of residual charge densities at the edge of EC molecules beyond the range of $W(\mathbf{r})/V_o$. (The net spin on EC^- is about 0.9 $|e|$ and is more centered on EC than the net charge.) Increasing w_i is ruled out because of the close proximity of adsorbed EC to the surface hydroxyl groups. For example, using larger w_i has been found to lead to abstraction of protons from surface hydroxyls. The protons then bind to the negatively charged EC molecule. Such reactions are not seen in unconstrained AIMD simulations and are deemed unphysical. We have therefore defined +0.20 $|e|$ and −0.60 $|e|$ to be the net charges of flat, intact EC and EC^- (Figure 4c and d, respectively) when using self-consistent cDFT calculations to impose charges on the molecule. Increasing $|V_o|$ to increase the charge on adsorbed EC^- to −0.80 $|e|$ is found to yield only a 10% change on the coupling matrix element V_{AB} but can increase λ by a fraction of an electron volt. The more important parameter, the barrier in eq 1, is only affected by $\sim\delta\lambda/4$ in the harmonic approximation used in this work. In the Supporting Information, the predicted λ for adsorbed EC is shown to be comparable to that for EC in liquid EC, computed using cluster calculations, localized orbitals, and a dielectric continuum approximation.

Coupling matrix elements V_{AB} between the two different adiabatic surfaces (Figure 1a) are computed using the cDFT formalism for discrete orbital levels,[39] which is implemented into VASP within the projector-augmented wave formalism.[68] The same atomic configuration must be used for both electronic surfaces, and this is chosen to be the optimized atomic configuration where no excess electron resides on the flat, adsorbed EC. V_{AB} is generally assumed to be relatively independent of atomic positions with the Franck−Condon approximation, although molecular orientation dependence has been demonstrated.[44] V_{AB} emerges from the 2 × 2 Hamiltonian matrix H connecting the donor ($|\Phi_A\rangle$, in our case from unconstrained DFT calculations) and acceptor ($|\Phi_B\rangle$) single determinantal wavefunctions.[39,72] Generated using cDFT, $|\Phi_B\rangle$ features an excess electron on one EC molecule. H contains the overlap matrix element $\langle\Phi_A|\Phi_B\rangle$ as well as $\langle\Phi_A|\Sigma_e W(r_e)|\Phi_B\rangle$, where e labels all occupied electronic levels.[39] These calculations are fairly costly and are performed at T = 0 K in this work.

This cDFT-based V_{AB} formulation was originally devised for electron transfer between ground-state cDFT donor and acceptor electronic configurations, with the implicit assumption that the relevant density-of-state (DOS) is discrete. In the limit of noninteracting electrons residing on a metal electrode, this formalism reflects only the top curve on the left side of Figure 1b and does not reduce to the well-known Fermi golden rule formula for tunneling from a continuum of donor states. Consider, in this limit, a band of single-particle energy levels E characterized by a DOS $D(E)$ of orbitals $\phi(E)$, Fermi distribution function $f(E)$, Fermi level E_F, and an isolated acceptor orbital ϕ_a with energy E_a. The golden rule rate, associated with multiple level crossings illustrated in Figure 1b, is

$$k_{GR} \propto \langle \int dE |\langle\varphi(E)|v(E)|\varphi_a\rangle|^2 D(E) f(E - E_F)\delta(E - E_a)\rangle_R \quad (4)$$

where $v(E)$ is the single-particle coupling matrix element and $\langle O\rangle_R$ denotes averaging over nuclear degrees of freedom R on which all quantities implicitly depend. This formula allows many-electron acceptor $|\Phi_{B'}\rangle$ states that involve ϕ_a but not the highest occupied molecular orbital (HOMO) of $|\Phi_A\rangle$, which represents electron−hole excitations.[52] In contrast, cDFT can only generate the electron-acceptor manifold $|\Phi_{B'}\rangle$ which is the ground electronic state within the applied constraint.

To incorporate the effect of eq 4, we make the common assumption that V_{AB} is constant over the relevant range of DOS.[46−55] Then an empirical golden rule-like expression can

be proposed

$$k_{et}^{GR} = \sum_{a'} f_{a'} \frac{\sqrt{\pi}|V_{AB}|^2}{\hbar\sqrt{\lambda k_B T}} \exp\left[-\frac{(\Delta E_o + \Delta E_{a'} + \lambda)^2}{4\lambda k_B T}\right] \quad (5)$$

Here ΔE_o is used in place of ΔG_o because we ignore entropy changes in T = 0 K, UHV-setting calculations, $f_{a'}$ is the Fermi and/or symmetry weight of Kohn−Sham orbital a′, and $\Delta E_{a'}$ is the difference in energy between the Fermi energy and each Kohn−Sham orbital level a′, $e_F - e_{a'}$; a′ deep within the occupied manifold does not contribute due to the $\Delta E_{a'}$ factor. The self-consistent Γ-point electronic density is used to generate a dense grid of occupied states $\phi_{a'}$ using a 1 × 4 × 4 Monkhorst−Pack Brillouin sampling.[73]

To converge to the infinite size limit for e^- transfer to a single EC molecule, the correct approach is not to increase *k*-point sampling but to increase all spatial dimensions of the model electrode. If the Li_xC_6 component of the electrode is doubled in size in any one direction, the orbital donor wave function $\phi_{a'}$ delocalized over the electrode is scaled down by $\sim 1/\sqrt{2}$, and $|V_{AB}|^2$ decreases 2-fold. This underscores the fact that V_{AB} is not a measurable quantity in finite-sized electrode models but changes with the system size. However, the DOS $D(E_{a'})$ increases proportionately with system size, and the sum over all orbital contributions (eq 5) should be well-defined in that infinite size limit.

D. Experimental Details. Carbon films deposited onto Cu were used as electrodes to explore the passivating role of the ALD-derived alumina coatings with respect to electrolyte reductive decomposition. Polished AT-cut quartz crystals patterned with Cu electrodes (9 MHz, Inficion) were used as the base current collector for conducting both voltammetry and gravimetry. Using a pulsed laser deposition method, 50 nm thick carbon films were deposited onto these crystals.[74,75] Conformal alumina coatings were deposited onto both carbon films and bare Cu electrodes at a substrate temperature of 180 °C using alternate cycles of trimethylaluminum and water to produce amorphous Al_2O_3 films of either 0.55 or 1.1 nm thickness.[11,76,77] Cycles of NO_2 and TMA pre-exposure were used to ensure the nucleation and growth of a continuous alumina film.[78] Electrochemical measurements were conducted under argon in a glovebox (Vacuum Atmospheres, <100 ppb H_2O, <1 ppm O_2) in 1 M LiPF6 in a 1:1 volume mixture of EC and diethylcarbonate (Hoshimoto and Kishida Chemical). A Solartron 1287 potentiostat coupled with a Maxtek RQCM controller were used for simultaneous voltammetric and gravimetric measurements.

III. RESULTS: ADIABATIC AIMD/DFT PREDICTIONS OF EC/LI (100) REACTIONS

Adiabatic DFT/PBE calculations should be pertinent for the EC/Li (100) interface, where EC and the metallic electrode are in close contact and fast e^- transfer is expected.

A. Liquid EC on Li (100). Liquid EC has been previously predicted to decompose at the C═O edges of LiC_6 electrodes within 7 ps at T = 450 K in AIMD/PBE simulations.[21] This time scale is used to qualitatively gauge the DFT/PBE predicted reactivity of other surfaces toward liquid EC.

Figure 2b shows that liquid EC decomposes readily on Li (100). Within 15 ps, all 12 EC molecules adjacent to the Li metal, out of 32 EC in the simulation cell, have accepted electrons and decomposed. Eleven out of these 12 exhibit two broken C_C−O bonds to form CO + $OC_2H_4O^{2-}$;[23−26] only one EC decomposes

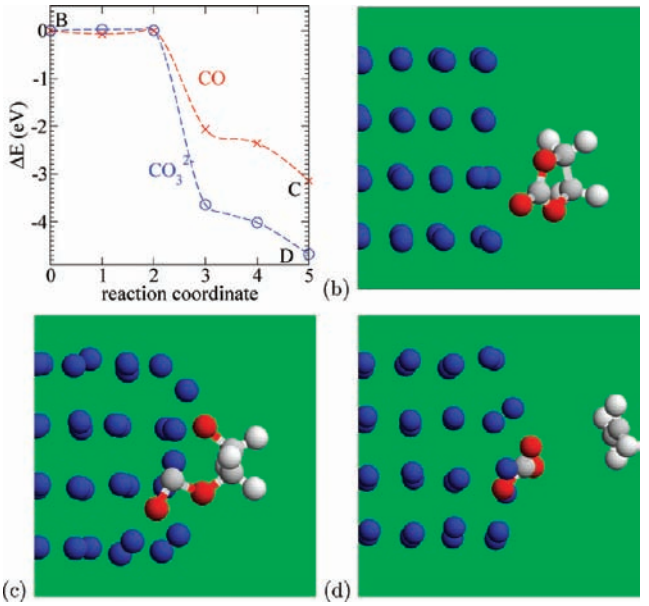

Figure 3. (a) Static, nudged elastic band (NEB) calculations of energy barriers associated with two modes of EC breakdown, producing CO or CO_3^{2-}, at T = 0 K. Points B−D correspond to panels (b−d). (b) Intact EC on Li (100). (c) EC partially decomposed into $OCOC_2H_4O$, precursor to CO and $OC_2H_4O^{2-}$, on Li (100). (d) CO_3^{2-} and C_2H_4 products on Li metal. The color key is the same as in Figure 2.

in the classic C_2H_4 + CO_3^{2-} route hitherto widely accepted in the literature, cleaving both C_E−O bonds.[1,2] Here C_C and C_E are the carbonyl and ethylene carbon atoms, respectively. This finding is consistent with those in ref 21, where both CO and CO_3^{2-} products emerge at the interface between liquid EC and pristine LiC_6 with oxidized edge groups. This agreement is significant because, by construction, the models used in ref 21 exclude solvent cointercalation cited in the "three-dimensional" SEI formation pathway.[66] Nevertheless, fast EC decomposition and identical products are predicted on both pristine graphite and Li metal surfaces, showing that such cointercalation is not necessary for SEI initiation.

In the EC/Li trajectory, the temperature is thermostat at T = 350 K, not T = 450 K, to avoid melting the solid Li. Despite this, the heat generated by the reactions and the incorporation of CO into the metal slab have caused significant amorphization. In ref 15, the initial 200 fs of this trajectory is examined in detail. The bent EC geometry, with the carbonyl C═O displacing out of the EC plane, is shown to be correlated with electron transfer to EC, just like for the isolated EC^- in solution (Figure 1d).[12,15] This bent geometry plays a critical role in electron-transfer and reorganization energy calculations in $LiAlO_2$-coated surfaces (see below). Our AIMD simulations have shown that $OC_2H_4O^{2-}$ can react with 2 CO_2 to form the main SEI organic product ethylene dicarbonate. Whether this product is deposited at the initial stage of SEI growth depends on the availability of CO_2 and the solubility of the decomposition fragments.[79]

B. Isolated EC on Li (100). Remarkably, even a single EC molecule, in the absence of the liquid environment which stabilizes its ionic breakdown products, still decomposes on Li (100) surfaces to form CO + $OC_2H_4O^{2-}$ within picoseconds (Figure 2c). This suggests that a simple T = 0 K energy profile calculation is relevant to EC decomposition.[80]

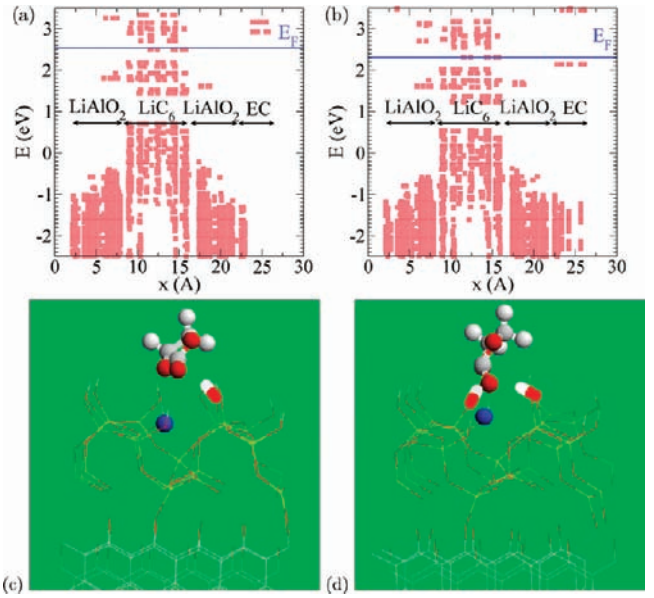

Figure 4. (a and b): Local electronic DOS decomposed along the *x*-axis (perpendicular to interface) for EC adsorbed on thin $LiAlO_2$-coated LiC_6. Panels (a and b) correspond to the configurations depicted in panels (c) (flat EC geometry) and (d) (bent geometry), respectively. The red patches depict integrated up- and down-spin densities exceeding 0.01 $|e|$ for each plane wave function collapsed on an atom centered at *x*. Panel (b) shows that the bent geometry drastically changes the HOMO and LUMO levels, with an excess electron now residing on EC below the Fermi level (E_F). The conduction band of the $LiAlO_2$ region is located above 4 eV. In panels (c and d), the EC molecule and Li coordinated to the EC are depicted as spheres, while surface hydroxyl groups donating hydrogen bonds to the EC are stick figures. Other Li are omitted, and all other oxide-coating and graphite atoms appear as wireframes. EC configurations on the thick $LiAlO_2$ coating are qualitatively similar (not shown). The color scheme is the same as in Figure 2.

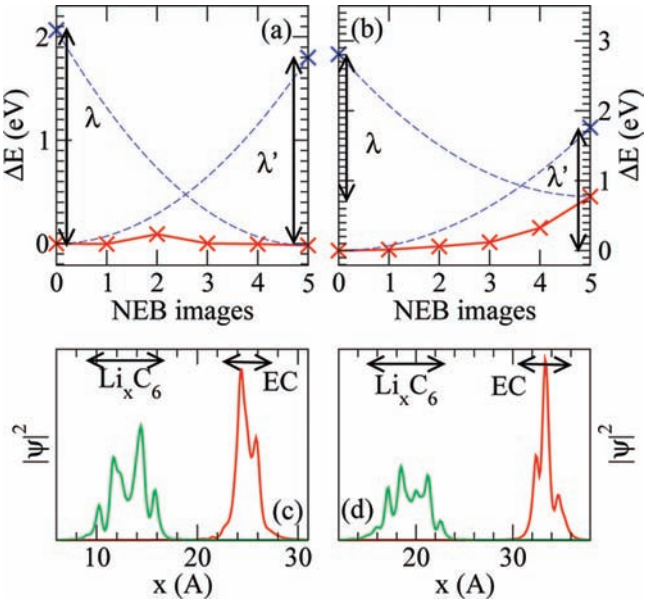

Figure 5. (a and b) Adiabatic and nonadiabatic (red and blue crosses, respectively) energy profiles along the reaction coordinate between the flat (Figure 4c, image "0") and the bent (Figure 4d, image "5") EC geometries when applying a 0.4 V/Å applied electric field to the 7 and 10 Å thick $LiAl_2O$ layers. Adiabatic energies are computed along the NEB-generated chain with unconstrained DFT. Nonadiabatic reorganization energies (λ) derive from cDFT. The dashed curves are parabolic fits. (c and d) Highest occupied orbital of the system (green) and the cDFT-computed e^--accepting EC orbital (red) adsorbed on the 7 and 10 Å thick $LiAl_2O$ layers, integrated over the lateral dimensions.

Figure 3a compares the T = 0 K energy profiles of the two modes of excess electron-induced EC breakdown on Li metal. They show that cleaving the C_C—O bond to form the precursor to carbon monoxide, $OC_2H_4OCO^{2-}$, is thermodynamically less favorable than the ethylene carbon—oxygen bonds to form CO_3^{2-} and C_2H_4 by a substantial 1.53 eV. Cleaving the remaining C_C—O bond in the CO route only leads to another 0.16 eV stabilization. The barriers associated with both types of bond breaking are vanishingly small. Applying the HSE06 truncated hybrid functional,[81,82] which exhibits far less self-interaction errors[32−34] than PBE, increases the C_C—O breaking barrier but only to 0.16 eV (not shown, but consistent with the similar short time dynamics predicted with the PBE and HSE06 functionals).[15] This suggests that adiabatic DFT/PBE barrier predictions are reasonably accurate for EC in contact with Li metal. The small barrier explains why both product channels are available in picosecond time scales at explicit liquid EC/electrode interfaces (Figure 2b, ref 15). We speculate that the kinetic prefactor favors the CO route and makes it the majority product in liquid—solid interface simulations (Figure 2b).

C. Long-Range e^- Transfer Formalism Is Not Applicable to EC/Li(100). For e^- transfer to EC directly adsorbed on uncoated electrode surfaces, the close contact should render the cDFT method for nonadiabatic long-range electron transfer[39,43] inapplicable. If one insists on calculating V_{AB} using cDFT and the simulation cell described in Table 1, then V_{AB} is found to be 0.23 eV for a flat EC adsorbed on Li (Figure 3b). This large V_{AB} is consistent with a significant, 56% overlap between the acceptor and the donor many-electron wave functions and should put the system in the adiabatic electron transfer regime—even with the caveat about the system size dependence of V_{AB}.[83] (For comparison, a theoretical work on NO molecules adsorbed on Ag (111), not using cDFT, has also yielded fraction of eV V_{AB}.[48]) We conclude that the adiabatic DFT/PBE treatment should suffice in this case.

IV. RESULTS: NONADIABATIC ELECTRON TRANSFER TO EC ON OXIDE SURFACES

This section focuses on a UHV-like model consisting of an isolated EC adsorbed on the lithium-intercalated graphitic carbon strip coated with $LiAlO_2$. A 0.4 V/Å electric field is applied. For this model, e^- tunneling resides in the nonadiabatic regime where cDFT calculations are pertinent. The relevance of this model to the liquid EC/electrode interfacial environment will be clarified below.

A. Two Metastable EC Charge States on 7 Å Thick Oxide Surface. The Li_xC_6 model with a 7 Å thick $LiAlO_2$ coating proves especially useful for examining the details of electron transfer from the electrode to an adsorbed EC, which either precedes or takes place simultaneously with EC^- decomposition. Two (meta)-stable adsorbed EC configurations can be stabilized (Figure 4). One is a flat, charge-neutral EC coordinated to a surface site (an AlOH group) via its carbonyl oxygen atom (Figure 4c). Figure 4a depicts the local electronic DOS for this system. The Li_xC_6 region contains partially occupied states near

the Fermi level (E_F). The insulating oxide spans a substantial band gap, although there are surface states in the interface with Li_xC_6 that reduce the effective insulating thickness. The HOMO of EC is below −2.5 eV, while the lowest unoccupied molecular orbital (LUMO) lies above E_F. This DOS is consistent with a charge-neutral EC weakly interacting with the oxide surface.

The other configuration has an intact EC^- which adopts a bent geometry with the C═O bond protruding out of the EC plane (Figure 4d). This is reminiscent of the first stage of liquid EC decomposition on Li (100) surface, where the e^--accepting EC adopts a similar bent configuration.[15,84] The excess charge on the EC is centered around the carbonyl oxygen atom, which is coordinated to two AlOH groups and a Li surface atom. The system exhibits a DOS (Figure 4b) substantially different from Figure 4a. The majority spin, highest occupied state of the EC molecule now lies below the Fermi level. The shift in the LUMO upon e^- addition serves as a caveat against using the LUMO of the neutral molecule as a figure-of-merit in assessing electrochemical reduction tendencies.

The bent EC^- is almost iso-energetic with the flat EC. Its slight exothermicity, $\Delta E_o = -0.02$ eV, does not depend on whether the electron transfer is adiabatic or nonadiabatic. It should not be affected by the periodic images imposed by the simulation cell because the dipole correction is applied.[71] In fact, despite the transfer of an e^- across a 7 or 10 Å thick oxide layer, the overall dipole moment of the simulation cell changes by less than 1.0 $|e|$Å, apparently because the electron density in the metallic Li_xC_6 strip can rearrange itself to accommodate the electron transfer. The total charge in the simulation cell is conserved in these calculations, and the large correction due to periodic boundary conditions for isolated ions in solutions is not needed.[85,86] Note that ΔE_o is used in place of ΔG_o because the calculation is performed at $T = 0$ K.

B. Nonadiabatic Electron Transfer on Oxide Surface. We apply the cDFT method to calculate λ and V_{AB} required to estimate the electron transfer rate k_{et} (eqs 1 and 5). We stress that the flat EC absorbed on the oxide coatings is treated using unconstrained DFT/PBE. The highest occupied orbitals of the 7 and 10 Å thick coatings reside in the Li_xC_6 region and exhibit integrated electron densities of less than 10^{-4} and 5×10^{-8} $|e|$ on the EC molecule, respectively. This shows that the unconstrained DFT method already gives a reasonable description of the neutral EC electronic configuration.

The λ is computed for the optimized, flat EC geometry adsorbed on the thin $LiAlO_2$ coating (i.e., image 0 in Figure 5a). cDFT imposes an extra electron on the EC molecule. On the 7 Å thick coating, it yields a vertical excitation energy $\Delta E_{vert} = \lambda + \Delta E_o = 2.04$ eV, where ΔE_o is the aforementioned −0.02 eV offset between donor and acceptor. Alternatively, an electron can be removed from the frozen bent EC^- configuration (image 5), which leads to $\lambda' + \Delta E_o = 1.80$ eV; λ and λ' agree to within 14%. This is qualitatively consistent with the Marcus theory postulate that the polarization degrees of freedom respond harmonically (eq 1), yielding a single reorganization energy that governs electron transfer reactions.[31] With $\lambda = 2.06$ eV for EC adsorbed on the thin $LiAlO_2$ surface, the nonadiabatic barrier becomes 0.51 eV from a simple Marcus construction (eq 1). This barrier is much higher than the ∼0.1 eV adiabatic DFT/PBE activation energies for both the C_C−O and C_E−O bond-breaking pathways on this surface (Section IVC) and is therefore the rate-limiting step in EC breakdown on the surface of the thin $LiAlO_2$ coating.

Table 2. Work Function of Model Systems Used in This Work Computed Using the PBE Functional, in eV[a]

coated electrode		uncoated electrode	
system	work funct.	system	work funct.
thin $LiAlO_2$ (OH)	2.47	Li(100)	3.05
thick $LiAlO_2$ (OH)	2.90	graphite edge	4.57
thin $LiAlO_2$ (OLi)	2.25	$LiAlO_2$	5.42
Al2O3 (OH)	4.10	Al_2O_3 (0001)	6.22

[a] The left column describes the oxide coatings on Li_xC_6, and the right column refers to work functions of pure crystals. The Al_2O_3 (0001) model is Al terminated. The graphite slab has dangling bonds.

In the Supporting Information, an EC with a dielectric approximation of the liquid EC solvent medium is found to exhibit an average of $\lambda = 1.76$ eV, similar to EC adsorbed on the thin $LiAlO_2$ coating. The cosolvent dimethyl carbonate (DMC) exhibits only slightly smaller λ values. Therefore the substantial λ, large compared to many organic molecules,[87] is intrinsic to out-of-plane bending of the C═O group, as the carbonyl carbon atom adopts a sp^3-like geometry to accommodate an e^-. The Supporting Information further presents results on vertical excitation energy, $\Delta E_{vert} = \lambda + \Delta E_o$ (Figure 1a), computed in several AIMD snapshots, to suggest that the Arrhenius term in eq 1 favors e^- transfer to EC molecules at the interface over EC in the bulk liquid region. In such AIMD simulations, we are limited to the first choice of λ, i.e., instantaneously adding an electron to EC, because EC^- in liquid EC can have short lifetimes.[21] Hence we will focus on this first choice throughout this work.

As this is a $T = 0$ K calculation in a UHV-like setting, we have simply used the $(\Delta E_o + \lambda)^2/(4\lambda)$ expression in eq 1 as the tunneling barrier[39,42] and have not traced out the two adiabatic curves as a function of the energy gap using liquid state potential-of-mean-force simulations.[88,89] We have however checked that, when relaxing EC^- frozen in the flat geometry (Figure 4c) with a constrained charge, it reverts to the stable bent EC^- (Figure 4d) configuration, showing that the cDFT approach puts the system on the correct electron-acceptor potential surface. In the future, we plan to perform direct cDFT calculation of the barrier height at $T = 0$ K by simultaneously optimizing the same atomic configuration on both energy surfaces.

The cDFT coupling matrix element is estimated to be $V_{AB} = 0.022$ eV at the flat EC geometry. Figure 5c depicts the highest occupied DFT and cDFT orbitals, integrated over the lateral dimensions, for the systems with flat EC and flat EC^-, respectively. The overlap between them, $\langle \phi_{EC}^{HOMO} | \phi_{EC^-}^{HOMO} \rangle$, is 0.0125 or within 2% of that between the respective determinantal wave functions $\langle \Phi_A | \Phi_B \rangle$ (Section II), which includes many-electron contributions. Therefore the relaxation of other electrons ("polarization effect") does not strongly influence the overlap integral when using Γ-point sampling.

This estimate of V_{AB} does not reflect the classic Fermi golden rule phenomenology (Section II). Applying eq 5 to approximately account for the finite DOS on the electrode, we obtain a 1.63×10^4/s electron-transfer rate. Simply using the cDFT definition of V_{AB} in eq 1, which represents a single point integration quadrature, merely underestimates this rate by a factor of 1.68. Using DFT/PBE rather than more accurate but costly hybrid functionals has been known to overestimate V_{AB} by almost a factor of 10.[44] In the present case, the DFT/PBE

underestimation of the band gap of the insulating oxide layer may lead to some overestimation of the electron tunneling rate. Despite the approximations and the assumptions involved, this is to our knowledge the first DFT-based estimate of the tunneling rates from an electrode, through an oxide layer, to an adsorbed EC molecule. The value may potentially be compared with UHV measurements. After electron transfer, EC^- decomposes, and the negatively charged EC fragments will most likely complex with Li^+ from the electrolyte and be incorporated into the SEI layer on top of the ALD film.

On the thicker $LiAlO_2$ coating, ΔE_o = 0.77 eV. In the flat EC geometry, λ=1.98 eV is predicted. Removing an e^- from the bent geometry yields λ' = 1.69 eV. The asymmetry is 15%. We again adopt the first choice of λ. V_{AB} is estimated at 0.0128 eV, about half that of the 7 Å thick $LiAlO_2$ coating.[90] As discussed in Section IVE, the thinner coating exhibits substantial surface relaxation which is absent in the 10 Å layer, making a purely thickness-based comparison of V_{AB} difficult. Figure 4d depicts the donor and the acceptor Kohn−Sham and cDFT orbitals. The overlap between them, $\langle\phi_{EC}|\phi_{EC^-}\rangle$, is about 0.004, a factor of 3 less than that across the 7 Å thick coating. Including the contributions of eq 5, k_{et} becomes extremely small (2.8×10^{-5}/s) due to the larger ΔE_o.

The overall k_{et} is clearly very sensitive to ΔE_o or ΔG_o. In UHV settings, ΔE_o depends on both the electric field and the surface heterogeneity at atomic lengscales (see below). At electrode/liquid electrolyte interfaces, k_{et} is a function of the applied voltage as well as the local EC reduction potential via ΔG_o (eq 1), which may be a function of the distance from the electrode. Direct measurement of the reduction potential of an intact EC is unavailable because EC decomposition occurs faster than cyclic voltammetry time scales. If one adopts a theoretical ΔG_o=− 0.15 eV for e^- transfer to intact EC molecules in EC liquid in at Li(s)/Li^+ voltages (Supporting Information), then the predicted initial electron transfer rates k_{et} through the 7 and 10 Å thick oxide coatings ($\sim 1.7 \times 10^5$ and 8.3×10^4/s) will permit electrolyte breakdown, even if we assume that these rates are overestimated by 100 times due to the use of the PBE functional discussed above. Indeed, our gravimetric measurements reveal electrolyte decomposition on the coated electrodes—consistent with ready availability of electrons—albeit in much less quantity than on uncoated electrodes (Section V). The electrolyte decomposition product then yields an additional insulating layer that prevents further electron tunneling.

Our main point in this section is not to predict exact k_{et} values but to highlight the previously neglected role of the EC reorganization energy (λ) on electrode coated with an insulating layer. An immediate implication is that different solvent molecules/salt components may exhibit different λ and e^--transfer rates.

C. DFT/PBE Treatment of Electron Transfer on Oxide Surface Is Inadequate. We next demonstrate that adiabatic DFT/PBE calculations are inadequate when dealing with e^- tunneling through insulating oxide layers.

The electron-transfer barrier strongly depends on whether the e^- transfer is adiabatic or not and on the accuracy of the DFT method used. Figure 5a depicts a climbing image NEB calculation with four images along the reaction coordinate linking the flat EC and the bent EC^- to examine the DFT/PBE adiabatic energy landscape in the 0.4 V/Å electric field. DFT/PBE predicts a 0.09 eV barrier associated with electron transfer through the thin $LiAlO_2$ layer.

This small 0.09 eV value gives the strongest indication that DFT/PBE grossly underestimates the e^- transfer barrier. In classical electron-transfer paradigm (Figure 1a), the parabolic intersection which yields the nonadiabatic barrier in the exponential term in eq 1 is expected to differ from an adiabatic prediction of barrier by V_{AB}. Instead, the former is 0.51 eV, and the latter is 0.09 eV (Figure 5a); their difference far exceeds V_{AB} = 0.022 eV before considering system size dependence. The discrepancy is most likely due to the self-interaction error in the DFT/PBE functional,[32,34] a point already alluded to in ref 39. The widely used PBE functional, along with others, does not sufficiently penalize configurations where an electron occupies both the electrode and the EC molecule. Indeed, in image 2 of Figure 5a, a fractional −0.2 $|e|$ charge develops on the EC, which should be considered unphysical for a molecule separated from the electrode by at least 7 Å. Hybrid DFT functionals exhibit less self-interaction errors than DFT/PBE but are currently too costly for computing barriers in interfacial systems of this size.[35]

The 10 Å thick oxide-coated electrode exhibits a monotonic DFT/PBE energy profile for electron transfer. There is no DFT/PBE adiabatic barrier between the flat EC and the bent EC^- beyond the minimal 0.77 eV mandated by the endothermicity (Figure 5b), suggesting that the electron tunneling barrier is again severely underestimated. Using the conjugate gradient geometry minimizer in VASP, the bent EC^- geometry on this surface is in fact on the verge of instability, about to lose electron density to the electrode and relax to the flat EC^0 geometry. Therefore the depicted energy profile actually reflects an optimized geometry subject to a charge constrained via cDFT with a small V_o = −0.2 eV.

D. Work Function and Electrochemical Potential. The electron tunneling rate at electrolyte−electrode interfaces depends on the electrochemical potential (Φ) of the electrode. In the coated graphite model systems, Φ is not precisely known. Directly calculating Φ involves averaging the electrostatic potential difference between the conductive (inner) region of the electrodes and a distant point in the bulk liquid beyond the thickness of the electric double layer[91] and involves consideration of image charge and surface potential effects.[86,92−94] These are beyond the time and length scales of current AIMD simulations. Fortunately, the EC/Li (100) interface mimics immersing freshly prepared Li metal into liquid EC and reflects an unambigous open-circuit voltage below the threshold at which EC becomes electrochemically decomposed [+0.8 V vs Li^+/Li(s)]. This is a major reason Li is considered in this work.

If we consider the energy of an e^- in the bulk electrolyte to be a constant, independent of electrode surfaces, the energy for ejecting an electron from different electrodes into the bulk electrolyte will only be shifted by the work function[95] (where an e^- goes into vacuum). Thus, we have computed the work functions of coated and uncoated electrode surface and some crystal planes of ALD coating materials (Table 2). The −OH and −OLi terminated $LiAlO_2$ coating work functions are within 0.5 eV of the Li metal value, indicating that similar energies are required to remove an electron from these surfaces. The Al_2O_3 coated surface has a much higher work function (Table 2), consistent with our observation that Al_2O_3 is a more insulating material than $LiAlO_2$ (see below).

Even though our DFT calculations show that placing these oxides in contact with Li metal surfaces leads to immediate Li metal oxidation, we use Li (100) as a reference because its voltage is similar to that of LiC_6. Aligning the work functions of Li (100) and the oxide materials (Table 2), it is clear that the valence and

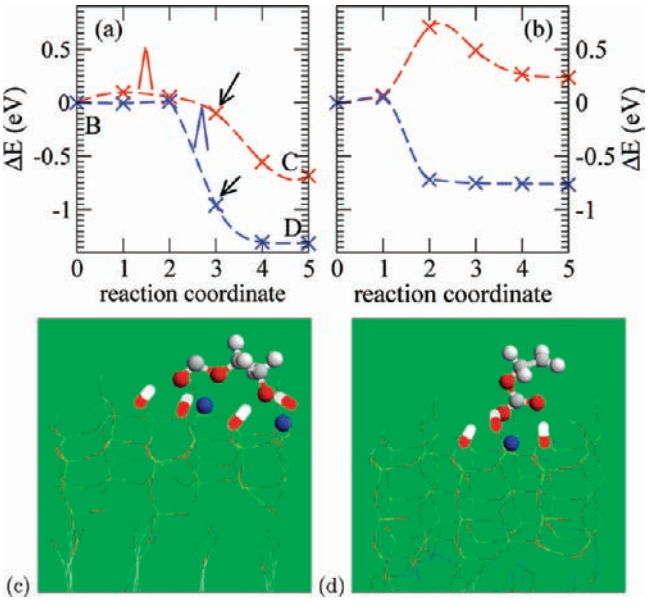

Figure 6. (a) Adiabatic DFT/PBE energy profiles associated with EC decomposition on the thin $LiAlO_2$ coating at $T = 0$ K. Red and blue refer to adsorbed $OCOC_2H_4O^{2-}$ and $C_2H_4OCO_2^{2-}$ intermediates, which are precursors to CO and CO_3^{2-} products, respectively. The electric field strength is 0.4 V/Å. The dashed lines are guides to the eye. Red and blue triangles depict the barrier associated with the first transfer of an electron on to the EC molecule, which is detected between images. They indicate that the DFT/PBE treatment erroneously neglects the electron tunneling barrier. Black arrows denote first detection of C−O bond breaking in an image. Point B corresponds to the intact EC in Figure 4c. (b) Same as (a) but for a single 10 Å thick layer in the absence of Li_xC_6 or electric field. (c and d) $OCOC_2H_4O^{2-}$ and $C_2H_4OCO_2^{2-}$ on thin $LiAlO_2$ surfaces, corresponding to points C and D in panel (a). The atom representation is the same as in Figure 4.

conduction bands of the ALD phase lie below and above the Fermi energy (E_F) of Li metal, respectively. Electron tunneling from the Li E_F to the conduction bands of Al-terminated Al_2O_3 (0001) and $LiAlO_2$ (100) exhibits 1.43 and 1.13 eV offsets (barriers, ΔE), respectively.

According to the one-dimensional WKB formula, the tunneling prefactor is

$$k_{et} \propto \exp(-2\sqrt{2m_e\Delta E}R/\hbar) \quad (6)$$

where m_e is the electron mass. If we take a tunneling transmission probability of e^{-40} as the limit of vanishing electron tunneling, then 3.7 nm thick $LiAlO_2$ and 3.2 nm thick Al_2O_3 are required to stop total SEI growth using DFT/PBE predicted ΔE. The work function is only one contribution to Φ and does not contain solvent orientation and electric double-layer effects[96] (which should be less important for our inner-shell redox reduction of solvent compared to the classical paradigm of electron transfer to well-solvated outer-shell ions). Nevertheless, it gives a simple guidance for comparing different insulating ALD coating materials. As e^- transfer slows down and becomes rate limiting, the composition of SEI films formed from electrolyte decomposition will likely change. This is because solvent molecules (other than EC), the counterions (PF_6^-) in the salt, and other partially decomposed products may exhibit smaller electron-transfer barriers (reorganization energies) and start dominating the product channel.

E. EC Bond Breaking on ALD Coating After e^- Transfer. On the 10 Å thick $LiAlO_2$-coated Li_xC_6 strip (Figure 2f), no EC decomposes within 7 ps. The limited duration of the AIMD trajectory does not permit an estimate of the adiabatic AIMD/PBE free energy barrier. While this barrier can be computed using the AIMD/potential-of-mean-force method,[17] it will be underestimated due to PBE self-interaction errors and underestimation of the electron tunneling barrier.

However, on the 7 Å thick $LiAlO2_2$ layer, a C_C−O bond on one EC molecule is spontaneously broken within 1 ps (Figure 2e), yielding $OCOC_2H_4O^-$, the majority predicted product on Li metal surfaces (Figure 2b) and a precursor to CO. Here the monovalent anion intermediate is stabilized by hydrogen-bond donation from several AlOH groups and by coordination to two surface Li atoms. Since the DFT/PBE method erroneously underestimates the 0.51 eV e^- tunneling barrier associated with molecular reorganization (Figure 4a) which precedes bond breaking, it vastly overestimates the overall bond-breaking rate. Indeed, the EC decomposition time scale predicted with DFT/PBE is similar similar to the time scale predicted in the absence of the ALD layer.[21] This is in disagreement with our experimental measurements which reveal far less solvent decomposition products when an ALD layer is present (Section V). Instead, 0.51 eV should be taken as the overall activation energy in these bond-breaking events. With this barrier, the bond-breaking rate should occur in millisecond, not picosecond, time scales at room temperature. Nevertheless, this PBE-based AIMD calculation is valuable because it identifies the most reactive surface site. An EC adsorbed at this site is used in the e^- transfer calculation of the previous section (Figure 4). Under UHV-like conditions, an isolated EC molecule adsorbed at this site exhibits <0.05 eV adiabatic DFT/PBE C−O bond-breaking barriers, provided a 0.4 V/Å electric field is applied (Figure 6). The qualitative correspondence between adiabatic AIMD/PBE decomposition rate and UHV barrierless reaction is the reason this model is adopted for e^- transfer studies in Section IVB.

Because of its extreme thinness, optimizing the 7 Å thick $LiAlO_2$ film coated on to Li_xC_6 has caused 2 Li atoms per surface to migrate outward (Figure 2e). These outlying Li coordinate to the surface hydroxyl groups, polarizing them. The EC that undergoes breakdown (Figure 6d) is indeed hydrogen bonded to a OH group coordinated to a surface Li^+. Such Li migration to the surface does not occur in the thicker $LiAlO_2$ coating. Hence the faster adiabatic AIMD/PBE EC decomposition dynamics on the thin $LiAlO_2$ coating is not just a consequence of oxide thickness but is partly due to active site chemical specificity. This anomaly may also be the reason the predicted V_{AB} value does not strongly decrease with increasing the oxide thickness from 7 to 10 Å and may further explain the difference in work functions between Li_xC_6 coated with 7 and 10 Å thick $LiAlO_2$ films (Table 2).

The 10 Å thick $LiAlO_2$ coating does not exhibit outward Li atom migration. Here the DFT/PBE bond-breaking barriers of adsorbed EC are not readily deconvolved from e^- transfer (Supporting Information). For simplicity, we consider a model with just one 10 Å thick $LiAlO_2$ layer hydroxylated on both sides (Table 1), add one excess e^- that now always resides on the EC because of the Li_xC_6 e^- sink has been removed, and compute EC^- decomposition energetics without applied electric fields. C_E−O bond breaking to form CO_3^{2-} precurors remain barrierless and exothermic. However, the C_C−O cleavage route to form CO precurors becomes endothermic and exhibits a 0.71 eV

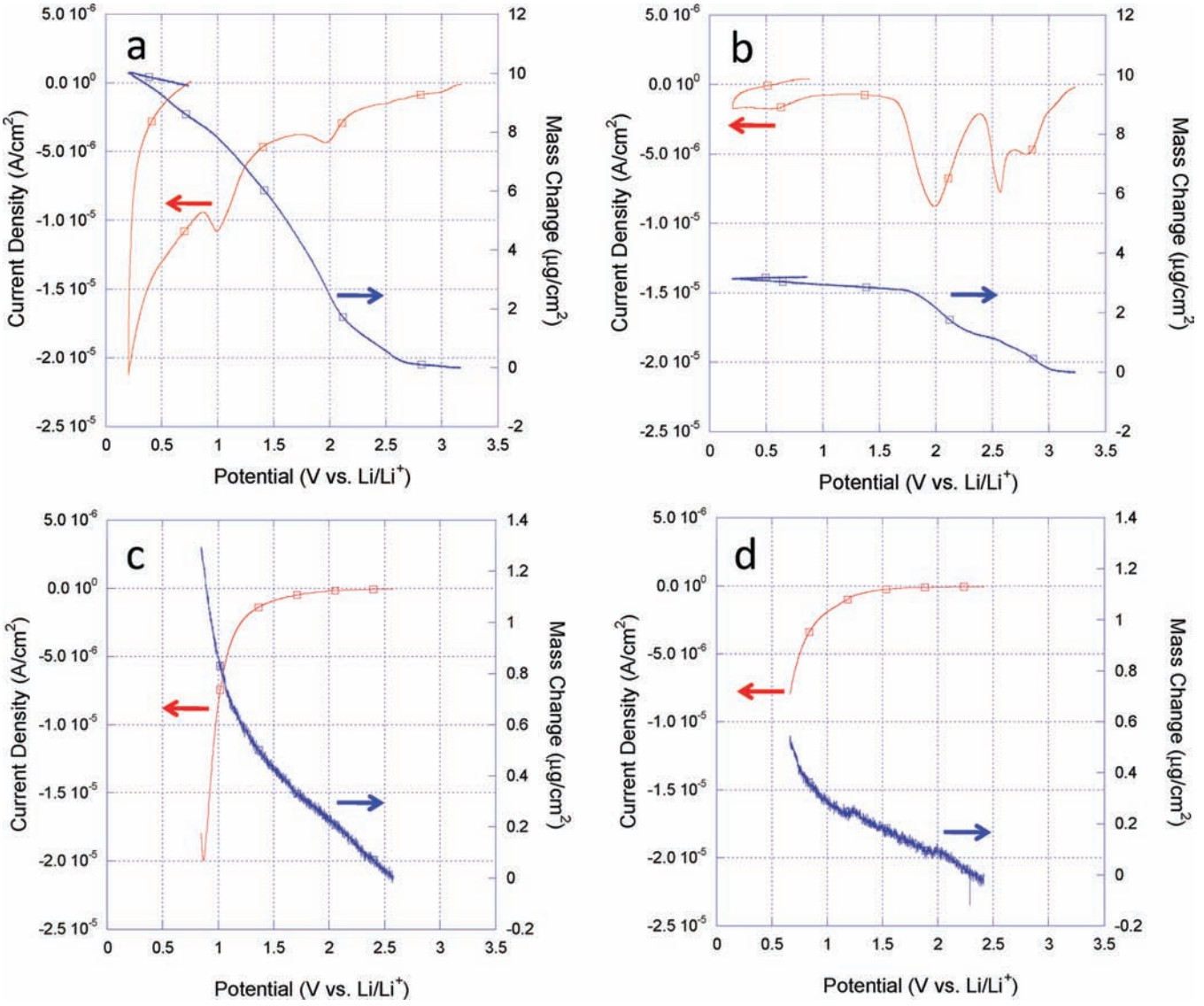

Figure 7. Current and mass change response with 1 mV/s^{-1} cathodic polarization of an electrode in 1 M LiPF6, 1:1 vol. EC:diethyl carbonate. (a) 50 nm C film, (b) Cu substrate without a C film, (c) 0.55 nm thick ALD Al_2O_3 on a 50 nm C film, and (d) 1.1 nm thick ALD Al_2O_3 on a 50 nm C film. Current and mass are normalized to the geometric area.

barrier. This indicates a product channel crossover as the oxide thickness increases and/or the reactivity of the surface site decreases. The expected reaction pathways transition from a mixture of C_E-O and C_C-O bond breaking to predominantly C_E-O cleavage (CO_3^{2-} precursor). While the liquid solvent environment is not included here, we speculate that this finding may be extrapolated to other coating surfaces, including natural SEI films, as the surface sites becomes less reactive. In the future, we will also examine EC decomposition reactions on Li_2CO_3 surfaces to see if similar trends persist on that crystalline material, recently adopted as a theoretical model for organic solvent decomposition SEI film,[30] and the decomposition of other solvent/salt molecules.

We have also conducted AIMD simulations of graphitic anodes coated with 5 Å thick hydroxylated Al_2O_3 layers (Figure 1f). No Li ions reside near the interface region, and no solvent decomposition is observed within 7 ps, despite the thinness of the oxide. This emphasizes the importance of surface heterogeneity at atomic length scales. Replacing all surface AlOH groups with AlOLi dramatically increases the decomposition rate; this will be discussed in future publications.

V. EXPERIMENTAL RESULTS

Figure 7 shows the combined voltammetric and microgravimetric responses of the uncoated and alumina-coated PLD carbon films as the electrode potential is decreased to a value slightly above the threshold for Li^+ intercalation in the carbon. The uncoated carbon electrode (Figure 6a) exhibits a continuously increasing current response, with several discrete maxima. One maximum reaches a value of 4 $\mu A/cm^2$ with a mass increase of 2 $\mu g/cm^2$ at a potential of 2 V. The other maximum reaches 11 μ/cm^2 at a potential of 1 V. The decomposition of the electrolyte and deposition of byproducts at 2 V is catalyzed by the Cu substrate, as evidenced by the similar current and mass changes on a control Cu electrode (Figure 7b) and demonstrates that the

dx.doi.org/10.1021/ja205119g |J. Am. Chem. Soc. 2011, 133, 14741–14754

carbon films possess porosity and allow electrolyte penetration. As seen in the limiting current and mass profiles of Figure 7b, electrolyte decomposition results in Cu passivation beyond 2 V, arguing that the majority of the current and mass changes measured above 2 V for the porous carbon films (Figure 7a) are due to electrolyte decomposition on Cu; only the signal below 1 V is associated with SEI formation on the carbon surface. The porous and therefore higher area carbon surface exhibits a continuous increase in both current and mass uptake, as the potential is further reduced from 2 to 0.2 V and the onset of Li^+ intercalation is approached. With an approach to 0.2 V, the rate of current change increases substantially over the rate of mass change, signaling a point where Li^+ intercalation has initiated, where the lighter mass Li (compared to an fragment of EC or diethyl carbonate) accounts for a growing fraction of the measured current. The possibility exists that current increase could also be related to solvent reduction without mass addition to the surface (soluble byproduct formation), but note that the mass decrease upon reversal of the potential sweep clearly argues for the onset of Li^+ ion intercalation into the carbon. We note that the scan rate of 1 mV/s is sufficiently fast to produce only modest extraction of Li during this reverse partial half cycle.

The alumina coating acts as a kinetic barrier to prevent electron transfer to the organic carbonate molecules of the electrolyte. Figure 7c and d show the response of 0.55 and 1.1 nm thick coated carbon films to the onset of electrolyte reductive decomposition. Comparison of the uncoated (Cu subtracted) and coated carbon films shows that a higher overpotential is required to drive solvent decomposition and a lower quantity of mass addition takes place with the alumina coating present. A Cu current and mass uptake response is eliminated for these coated electrodes because the alumina nucleating agent and film precursors fully penetrate the porous carbon, conformally coating both the carbon network and the underlying exposed regions of the Cu substrate. The onset for significant current density and mass increase occurs at approximately 1.2 and 0.8 V for the 0.55 and 1.1 nm alumina coatings, compared to 1.5 V for the uncoated carbon. Mass increases measured at 0.8 V are 6, 1.3, and 0.5 $\mu g/cm^2$ for the uncoated (Cu subtracted), 0.55 and 1.1 nm alumina sample, respectively. The greater overpotential and reduced mass uptake of the 1.1 nm coating relative to the thinner 0.55 nm coating argue that the thicker film provides a more effective kinetic barrier for reducing the extent of both reductive solvent decomposition and byproduct deposition on the electrode. The thicker alumina film would be expected to present a lower electron tunneling rate, resulting in a slower rate of solvent decomposition and retarded SEI formation. The fact that mass addition is observed in the presence of these alumina coatings is a clear indicator that alumina serves to retard and limit the extent but does not prevent electrolyte reduction and resulting byproduct film formation.

VI. CONCLUSIONS

In this work, we compare EC decomposition on Li metal and on models of oxide-coated electrodes. The latter mimics recent experimental work using ALD technique to passivate anodes. This ALD strategy carries significant technological promise,[6−11] and it also provides an ideal robust platform for theoretical and experimental study of passivating mechanisms. These two systems represent two electron-transfer regimes.

On pristine Li (100) surfaces, liquid EC and even isolated adsorbed EC molecules are predicted to undergo decomposition in picosecond time scales. CO is the dominant product, possibly because of favorable kinetic prefactors, even though both the CO and CO_3^{2-} reaction pathways are almost barrierless and the CO_3^{2-} product is more thermodynamically stable. EC molecules and the electrode are in close contact and strongly coupled. Adiabatic DFT/PBE and AIMD/PBE simulations should be accurate in this regime.

In contrast, electron transfer through an oxide layer should be slow compared to nuclear motion. We find evidence that tunneling through even a 7 Å thick oxide layer belongs to the nonadiabatic regime. Applying cDFT calculations, such thin coatings are found to slow down e^- transfer because the solvent reorganization energy λ now figures prominently in electron tunneling through the oxide. Largely neglected in previous studies of electrolyte decomposition in batteries, λ is estimated to be ~2 eV for adsorbed EC molecules in ultrahigh vacuum-like conditions. This translates into a ~0.5 eV electron tunneling barrier within the harmonic approximation when the e^- transfer free energy change is small.

cDFT calculations show that the 7 and 10 Å thick $LiAlO_2$-coated Li_xC_6 exhibit electron-transfer rates of $\sim 10^5$/s at the Li^+/Li(s) applied voltage. The predicted e^- transfer rate is not free of ambiguities and assumptions and is of order-of-magnitude utility; further fundamental research is needed for a more rigorous treatment. Despite this caveat, this work respresents the first first-principles estimate of the e^- tunneling rate between an electrode and an EC molecule across an insulating oxide layer. Such predictions are critical for understanding ALD-hindered SEI growth in lithium ion batteries.

The overall electron-transfer rate (eqs 1 or 5) also depends on the offset ΔG_o between e^- donor and acceptor species. ΔG_o in turn depends on the applied voltage. AIMD estimates of ΔG_o in an explicit liquid solvent environment are currently lacking, and we have relied on dielectric continuum treatments of the liquid environment. Nevertheless, our analysis yields useful insights. With any reasonable estimate of ΔG_o, the electron-transfer rate to EC at the surface is predicted to be faster than 1/s, and solvent breakdown on the ALD oxide is expected. This is confirmed by our gravimetric measurements on ALD-coated anodes, although the amount of solvent decomposition product is significantly less than that on uncoated graphite electrodes.

In the case of oxide-coated electrodes, AIMD/PBE and DFT/PBE calculations without electronic constraints vastly underestimate the electron-transfer barrier. The reason is most likely the self-interaction error, which unphysically favors a split electron partially localized on the EC and partially delocalized on the electrode. This defect exists in many DFT functionals and has been known to yield errors in when a molecule is split into two fragments.[32] As a result, direct AIMD/PBE simulations overestimate EC decomposition rates at oxide-coated electrode surfaces by many orders of magnitude. However, AIMD/PBE and DFT/PBE calculations still provide a wealth of information about structure and relative energetics, and they form the basis of Marcus theory considerations and nonadiabatic electron-transfer studies which are key aspects of this work.

Taking advantage of the qualitative correspondence between AIMD liquid-state reaction rates and ultrahigh vacuum-like DFT calculations of barrier heights at $T = 0$ K in an electric field, we have applied calculations in UHV-like settings to suggest that the dominant product from EC may shift from a mixture of CO and

CO_3^{2-} to mainly CO_3^{2-}, as the binding of ionic decomposition products becomes less favorable (e.g., on thicker oxide coatings). This prediction may be transferrable to natural SEI films, arising entirely from electrolyte decomposition. Atomic-scale surface heterogeneity is found to affect EC decomposition, with Li^+ ions at the surface playing a facilitating or "catalytic" role. Our work paves the way for novel future experimental studies in UHV settings.

■ ASSOCIATED CONTENT

Supporting Information. Reorganization energies of EC in bulk liquid, vertical excitation energies of EC at $LiAlO_2$/liquid EC interfaces, DFT/PBE predictions of adiabatic bond-breaking barriers, and discussions of possible $LiAlO_2$ stoichiometry on ALD Al_2O_3 coatings upon cycling power. This material is available free of charge via the Internet at http://pubs.acs.org.

■ AUTHOR INFORMATION

Corresponding Author
kleung@sandia.gov

■ ACKNOWLEDGMENT

We thank John Sullivan, Steve Harris, Na Sai, Anatole von Lilienfeld, and David Rogers for useful discussions, Michael Siegal and Donald Overmyer for the nanoporous carbon samples, and Xingcheng Xiao for sharing ref 60 prior to publication. Sandia National Laboratories is a multiprogram laboratory managed and operated by Sandia Corporation, a wholly owned subsidiary of Lockheed Martin Corporation, for the U.S. Department of Energy's National Nuclear Security Administration under contract DE-AC04-94AL85000. K.L. (apart from the work on lithium metal modeling) was supported by Nanostructures for Electrical Energy Storage (NEES), an Energy Frontier Research Center funded by the U.S. Department of Energy, Office of Science, Office of Basic Energy Sciences under award no. DESC0001160.

■ REFERENCES

(1) *Advances in lithium-ion batteries*; van Schalkwijk, W. A., Scrosati, B., Ed.; Kluwer: New York, 2002.
(2) *Lithium-ion batteries: solid-electrolyte interphase*; Wang, Y., Balbuena, P. B., Ed.; Imperial College: London, 2004.
(3) Xu, K. *Chem. Rev.* **2004**, *104*, 4304.
(4) Aurbach, D.; Ein-Eli, Y.; Chusid, O.; Carmeli, Y.; Babai, M.; Yamin, H. *J. Electrochem. Soc.* **1994**, *141*, 603. Aurbach, D.; Markovsky, B.; Shechter, A.; Ein-Eli, Y; Cohen, H. *J. Electrochem. Soc.* **1996**, *143*, 3809.
(5) Arora, P.; White, R. E.; Doyle, M. *J. Electrochem. Soc.* **1998**, *145*, 3647.
(6) Riley, L. A.; Cavanagh, A. S.; George, S. M.; Lee, S.-H.; Dillon, A. C. *Electrochem. Solid-State Lett.* **2011**, *14*, A29 (2011).
(7) Riley, L. A.; Cavanagh, A. S.; George, S. M.; Jung, Y. S.; Yan, Y. F.; Lee, S. H.; Dillon, A. C. *ChemPhysChem* **2010**, *11*, 2124.
(8) Jung, Y. S.; Cavanagh, A. S.; Dillon, A. C.; Groner, M. D.; George, S. M.; Lee, S.-H. *J. Electrochem. Soc.* **2010**, *157*, A75.
(9) Scott, I. D.; Jung, Y. S.; Cavanagh, A. S.; Yan, Y.; Dillon, A. C.; George, S. M.; Lee, S.-H. *Nano Lett.* **2011**, *11*, 414.
(10) Riley, L. A.; Van Atta, S.; Cavanagh, A. S.; Yan, Y. F.; George, S. M.; Liu, P.; Dillon, A. C.; Lee, S.-H. *J. Power Sources* **2011**, *196*, 3317.
(11) Jung, Y. S.; Cavanagh, A. S.; Leah, R. A.; Kang, S. H.; Dillon, A. C.; Groner, M. D.; George, S. M.; Lee, Y. H. *Adv. Mater.* **2010**, *22*, 2172.
(12) Wang, Y.; Nakamura, S.; Ue, M.; Balbuena, P. B. *J. Am. Chem. Soc.* **2001**, *123*, 11708.
(13) Han, Y. K.; Lee, S. U. *Theor. Chem. Acc.* **2004**, *112*, 106.
(14) Vollmer, J. M.; Curtiss, L. A.; Vissers, D. R.; Amine, K. *J. Electrochem. Soc.* **2004**, *151*, A178.
(15) Yu, J. M.; Balbuena, P. B.; Budzien, J. L.; Leung, K. *J. Electrochem. Soc.* **2011**, *158*, A400.
(16) Nair, N. N.; Schreiner, E.; Marx, D. *J. Am. Chem. Soc.* **2006**, *128*, 13815.
(17) Leung, K.; Nielsen, I. M. B.; Criscenti, L. J. *J. Am. Chem. Soc.* **2009**, *131*, 18358.
(18) Cheng, J.; Sprik, M. *J. Chem. Theory Comput.* **2010**, *6*, 880.
(19) Sulpizi, M.; Sprik, M. *Phys. Chem. Chem. Phys.* **2008**, *10*, 5238.
(20) Zipoli, F.; Car, R.; Cohen, M. H.; Selloni, A. *J. Am. Chem. Soc.* **2010**, *132*, 8593.
(21) Leung, K.; Budzien, J. L. *Phys. Chem. Chem. Phys.* **2010**, *12*, 6583.
(22) For AIMD simulations of electrolytes, see also: Del Popolo, M. G.; Lynden-Bell, R. M.; Kahanoff, J. *J. Phys. Chem. B* **2005**, *109*, 5895. Ganesh, P.; Jiang, D.; Kent, P. R. C. *J. Phys. Chem. B* **2011**, *115*, 3085.
(23) Onuki, M.; Kinoshita, S.; Sakata, Y.; Yanagidate, M.; Otake, Y.; Ue, M.; Deguchi, M. *J. Electrochem. Soc.* **2008**, *155*, A794.
(24) Ota, H.; Sakata, Y.; Inoue, A.; Yamaguchi, S. *J. Electrochem. Soc.* **2004**, *151*, A1659.
(25) Gachot, G.; Ribiere, P.; Mathiron, D.; Grugeon, S.; Armand, M.; Leriche, J.-B.; Pilard, S.; Laruelle, S. *Anal. Chem.* **2011**, *83*, 478.
(26) Marom, R.; Haik, O.; Aurbach, D.; Halalay, I. C. *J. Electrochem. Soc.* **2010**, *157*, A972.
(27) Ein-Eli, Y. *Electrochem. Solid-State Lett.* **1999**, *2*, 212. Aurbach, D.; Teller, H.; Levi, E. *J. Electrochem. Soc.* **2002**, *149*, A1255.
(28) Peled, E.; Menachem, C.; Bar-Tow, D.; Melman, A. *J. Electrochem. Soc.* **1996**, *143*, L4.
(29) Leong, M.; Doris, B.; Kedzierski, J.; Rim, K.; Yang, M. *Science* **2004**, *306*, 2057.
(30) To partially circumvent this problem, Li_2CO_3 crystals have been adopted as SEI models. See: Iddir, H.; Curtiss, L. A. *J. Phys. Chem. C* **2010**, *114*, 20903.
(31) Marcus, R. A. *Rev. Mod. Phys.* **1993**, *65*, 599.
(32) Cohen, A. J.; Mori-Sanchez, P.; Yang, W. T. *Science* **2008**, *321*, 792.
(33) Mori-Sanchez, P.; Cohen, A. J.; Yang, W. T. *Phys. Rev. Lett.* **2008**, *100*, 146401.
(34) Sai, N.; Barbara, P.; Leung, K. *Phys. Rev. Lett.* **2011**, *106*, 226403.
(35) Hybrid DFT functionals have been applied to frozen interfacial geometries comprising hundreds of atoms, but geometry optimization is much more costly there. See, e.g.: Sai, N.; Leung, K.; Chelikowsky, J. R. *Phys. Rev. B* **2011**, *83*, 121309.
(36) An oft-cited example of self-interaction error manifests itself in the dissociation of H_2^+ in the gas phase. The lone electron should reside on one of the H's as the two H nuclei become widely separated, but many DFT functionals predict half an electron on each.
(37) Prezhdo, O. V.; Kindt, J. T.; Tully, J. C. *J. Chem. Phys.* **1999**, *111*, 7818.
(38) Van Voorhis, T.; Kowalczyk, T.; Kaduk, B.; Wang, L. P.; Cheng, C. L.; Wu, Q. *Annu. Rev. Phys. Chem.* **2010**, *61*, 149.
(39) Wu, Q.; van Voorhis, T. *J. Phys. Chem. A* **2006**, *110*, 9212.
(40) Newton, M. D. *Chem. Rev.* **1991**, *91*, 767.
(41) Kuznetsov, A. M.; Ulstrup, J. *Electron transfer in chemistry and biology: an introduction to the theory*; Riley: Chichester, U.K., 1999; pp 214−217.
(42) Deskins, N. A.; Dupuis, M. *Phys. Rev. B* **2007**, *75*, 195212 our notation follows this work.
(43) Wu, Q.; van Voorhis, T. *Phys. Rev. A* **2005**, *72*, 024502.
(44) Oberhofer, H.; Blumberger, J. *J. Chem. Phys.* **2010**, *133*, 244105.

(45) Sit, P. H. L.; Cococcioni, M.; Marzari, N. *Phys. Rev. Lett.* **2006**, *97*, 028303.
(46) Behler, J.; Reuter, K.; Scheffler, M. *Phys. Rev. B* **2008**, *77*, 115421.
(47) Rogal, J.; Reuter, K.; Scheffler, M. *Phys. Rev. B* **2007**, *75*, 205433.
(48) Sharani, R.; Shenvi, N. A.; Tully, J. C. *J. Chem. Phys.* **2009**, *130*, 174716.
(49) Dogonadze, R. R.; Kuznetsov, A. M.; Levich, V. G. *Electrochim. Acta* **1968**, *13*, 1025.
(50) Schmickler, W. *J. Electronanal. Chem.* **1986**, *204*, 31.
(51) Halley, J. W.; Hautman, J. *Phys. Rev. B* **1988**, *38*, 11704.
(52) Sebastian, K. L. *J. Chem. Phys.* **1989**, *90*, 5056.
(53) Straus, J. B.; Calhoun, A.; Voth., G. A. *J. Chem. Phys.* **1995**, *102*, 529.
(54) Calhoun, A.; Koper, M. T. M.; Voth., G. A. *Chem. Phys. Lett.* **1999**, *305*, 94.
(55) Tanaka, S.; Hsu, C. P. *J. Chem. Phys.* **1999**, *111*, 11117.
(56) Kurth, S.; Stefanucci, G.; Almbladh, C.-O.; Rubio, A.; Gross, E. K. U. *Phys. Rev. B* **2005**, *72*, 035308.
(57) Hu, C.; Hirai, H.; Sugino, O. *J. Chem. Phys.* **2007**, *127*, 0641103.
(58) Tavernelli, I.; Curchod, B. F. E.; Rothlisberger, U. *J. Chem. Phys.* **2009**, *131*, 196101.
(59) Xu, K.; Xu, J.; Deng, P. Z.; Zhou, Y. Z.; Zhou, G. Q.; Qiu, R. S.; Fang, Z. J. *J. Cryst. Growth* **1998**, *193*, 127.
(60) Xiao, X. C., Lu, P.; Ahn, D. J. *Adv. Mater.* **2011**, DOI (DOI:10.1002/adma.201101915).
(61) Wyckoff, R. W. G. *Crystal Structures*, 2nd ed.; Interscience: New York, 1965; Vol.2, p 305.
(62) Marezio, M. *Acta Crystallogr.* **1965**, *19*, 396.
(63) Ouyang, C. Y.; Sljivancanin, Z.; Baldereschi, A. *Phys. Rev. B* **2009**, *79*, 235410.
(64) Bridel, J.-S.; Grugeon, S.; Laruelle, S.; Hassoun, J.; Reale, P.; Scrosati, B.; Tarason, J.-M. *J. Power Sources* **2010**, *195*, 2036.
(65) The reduction potential of $Li^+(EC) \rightarrow Li(s)$ should be similar to that of $Li^+(aq) \rightarrow Li(s)$ because the Li^+ solvation free energy in water and in EC are predicted to be similar, differing by at most 0.2 eV. See: Johansson, P.; Jacobsson, P. *Solid State Ionics* **2006**, *177*, 2691.
(66) Besenhard, J. O.; Winter, M.; Yang, J.; Biberacher, W. *J. Power Sources* **1995**, *54*, 228.
(67) Kresse, G.; Furthmüller, J. *Phys. Rev. B* **1996**, *54*, 11169. *Comput. Mater. Sci.* **1996**, *6*, 15.
(68) Kresse, G.; Joubert, D. *Phys. Rev. B* **1999**, *59*, 1758.
(69) Perdew, J. P.; Burke, K.; Ernzerhof, M. *Phys. Rev. Lett.* **1996**, *77*, 3865.
(70) Henkelman, G.; Uberuaga, B. P.; Jonsson, H. *J. Chem. Phys.* **2000**, *113*, 9901.
(71) Neugebauer, J.; Scheffler, M. *Phys. Rev. B* **1992**, *46*, 16067.
(72) Oberhofer, H.; Blumberger, J. *J. Chem. Phys.* **2009**, *131*, 064101.
(73) Our treatment of *k*-point sampling is qualitatively similar to: Schultz, P. A. *Phys. Rev. Lett.* **2006**, *96*, 246401. The cDFT orbitals in Figure 5c and d are isolated in energy from other orbitals. If a truly continuum of electronic states are used, then cDFT-based V_{AB} calculations would be difficult to implement.
(74) Siegal, M. P.; Yelton, W. G.; Overmyer, D. L.; Provencio, P. P. *Langmuir* **2004**, *20*, 1194.
(75) Siegal, M. P.; Overmyer, D. L.; Kottenstette, R. J.; Tallant, D. R.; Yelton, W. G. *Appl. Phys. Lett.* **2002**, *80*, 3940.
(76) Dillon, A. C.; Ott, A. W.; Way, J. D.; George, S. M. *Surf. Sci.* **1995**, *322*, 230.
(77) Ott, A. W.; Klaus, J. W.; Johnson, J. M.; George, S. M. *Thin Solid Films* **1997**, *292*, 135.
(78) Cavanagh, A. S.; Wilson, C. A.; Weimer, A. W.; George, S. M. *Nanotechnology* **2009**, *20*, 255602.
(79) Tasaki, K.; Harris, S. J. *J. Phys. Chem. C* **2010**, *114*, 8076.
(80) We stress that liquid EC does not exist at $T = 0$ K; only single adsorbed molecules can be investigated this way.
(81) Heyd, J.; Scuseria, G. E.; Ernzerhof, M. *J. Chem. Phys.* **2003**, *118*, 8207.Heyd, J.; Scuseria, G. E.; Ernzerhof, M. *J. Chem. Phys.* **2006**, *124*, 219906; Vydrov, O. A.; Heyd, J.; Krukau, A. V.; Scuseria, G. E. *J. Chem. Phys.* **2006**, *125*, 074106.
(82) HSE06 calculations are performed using VASP 5.2. See: Paier, J.; Marsman, M.; Kresse, G. *J. Chem. Phys.* **2007**, *127*, 024103.
(83) For $V_{AB} = 0.23$ eV and $\lambda \approx 2$ eV (predicted for EC adsorbed on electrode surfaces, Section IVB), the "transmission coefficient" $\kappa = 2P_{LZ}/(1 + P_{LZ}) = 14.4$, where P_{LZ} is the Landau−Zenner factor (see, e.g., ref 42). $\kappa > 1$ is associated with the adiabatic regime.
(84) A single EC^- embedded in dielectric continuum approximation of the liquid environment also exhibits such geometry (ref 12). See also the Supporting Information.
(85) VandeVondele, J.; Ayala, R.; Sulpizi, M.; Sprik, M. *J. Electroanal. Chem.* **2007**, *607*, 113. Tateyama, Y.; Blumberger, J.; Ohno, T.; Sprik, M. *J. Chem. Phys.* **2007**, *126*, 204506. Adriaanse, C.; Sulpizi, M.; VandeVondele, J.; Sprik, M. *J. Am. Chem. Soc.* **2009**, *131*, 6046.
(86) Cheng, J.; Sulpizi, M.; Sprik, M. *J. Chem. Phys.* **2009**, *131*, 154504.
(87) Coropceanu, V.; Cornil, J.; da Silva Filho, D. A.; Olivier, Y.; Silbey, R.; Bredas, J. L. *Chem. Rev.* **2007**, *107*, 926.
(88) Zeng, X. C.; Hu, H; Hu, X. Q.; Cohen, A. J.; Yang, W. T. *J. Chem. Phys.* **2008**, *128*, 124510.
(89) Moens, J.; Seidel, R.; Geerlings, P.; Faubel, M.; Winter, B.; Blumberger, J. *J. Phys. Chem. B* **2010**, *114*, 9173.
(90) The cDFT ground state for EC^- adsorbed on the thick $LiAlO_2$-coated electrode is a spin triplet. To compute V_{AB}, which requires the overlap integral $\langle\Phi_A|\Phi_B\rangle$, a triplet donor state $|\Phi_A\rangle$ is used. If we forcibly move the highest occupied orbital in the EC^- $|\Phi_B\rangle$ into the minority spin channel to overlap with the original singlet $|\Phi_A\rangle$, then the resulting V_{AB} is larger by 73%. This may be taken as an estimate of the uncertainty.
(91) Price, D. L.; Halley, J. W. *J. Chem. Phys.* **1995**, *102*, 6603.
(92) Lozovoi, A. Y.; Alavi, A.; Kohanoff, J.; Lynden-Bell, R. M. *J. Chem. Phys.* **2001**, 115.
(93) Pratt, L. R. *J. Phys. Chem.* **1992**, *96*, 25.
(94) Leung, K. *J. Phys. Chem. Lett.* **2010**, *1*, 496.
(95) Lang., N. D.; Kohn, W. *Phys. Rev.* **1971**, *3*, 1215.
(96) For another discussion of the relationship between Φ and the work function, see: Trasatti, S. *Sur. Sci* **1995**, *335*, 1. We stress that our focus of electron transfer to solvent molecules differs from the classical paradigm of outer-shell electron transfer to ions. Note that the experimental definition of "open circuit voltage" includes interfacial contributions, unlike some first-principles theoretical formulations.